Small Structures

small structures

www.small-structures.com

RESEARCH ARTICLE OPEN ACCESS

Highly Enhanced Directional Emission from Emitter-Integrated Dielectric Metasurfaces: Role of the Emitter Layer

Jungho Han[1] | Heejoo Jang[1] | Yugyeong Kim[1] | Jeheon Lee[1] | Young Chul Jun[1,2]

[1]Department of Materials Science and Engineering, Ulsan National Institute of Science and Technology (UNIST), Ulsan, Republic of Korea | [2]Graduate School of Semiconductor Materials and Devices Engineering, UNIST, Ulsan, Republic of Korea

Correspondence: Young Chul Jun (ycjun@unist.ac.kr)

Received: 10 December 2025 | **Revised:** 28 January 2026 | **Accepted:** 30 March 2026

Keywords: dielectric metasurface | directional light emission | emission enhancement | InP/ZnS quantum dot | low-loss emitter layer

ABSTRACT

Combining semiconductor quantum dots (QDs) with dielectric metasurfaces offers a promising platform for enhancing and controlling light emission properties. Highly enhanced directional and polarized emission is experimentally demonstrated from dielectric metasurfaces integrated with colloidal QDs. Specifically, emission enhancements from InP/ZnS QD- and CdSe/ZnS QD-integrated metasurfaces are directly compared. It is found that low absorption losses in the emitter layer can drastically increase the maximum achievable enhancement when different QDs are coated on the same metasurface. In particular, the lower intrinsic losses of the InP/ZnS QD layer enable dramatically enhanced vertical emission with narrow angular divergence, achieving a 140-fold enhancement in experiment. Our detailed experimental and theoretical investigations indicate the critical role of the emitter layer in the design of the emitter-integrated metasurface. Strong agreement between simulation and experiment confirms the critical-coupling behavior in maximized emission enhancement. Our study provides general guidelines for the development of directional light sources. Compact light sources with high directionality and controlled polarization hold strong potential for applications in displays, optical communications, sensing, and imaging.

1 | Introduction

Directional light sources are highly desirable in applications that require high radiance, controlled angular spectra, efficient waveguide coupling, or long-range light propagation [1–6]. They have become essential components in advanced displays, optical communications, optical sensing, and imaging systems. For example, directional light sources can be particularly advantageous for near-eye display technologies such as augmented reality (AR), which often rely on coupling light into waveguides or optical combiners with narrow angular acceptance windows [7–9]. Directional emission with small divergence angles improves coupling efficiency into these waveguide components without the need for bulky external optics. In addition, strong emission enhancement in the target direction is critical for AR, where computer-generated imagery must be overlaid onto bright natural scenes.

In this regard, integrating light emitters with dielectric metasurfaces offers a promising platform for enhancing and controlling emission properties. Dielectric metasurfaces are ultrathin, artificially engineered films composed of periodic arrays of high-refractive-index dielectric nanostructures [10, 11]. In recent years, they have emerged as highly versatile platforms in nanophotonics [4, 12–18]. Because they typically employ low-loss dielectric materials, dielectric metasurfaces can support high-quality (high-Q) optical resonances [19–22]. When emitters are integrated with such resonant structures, their emission can be significantly enhanced. Beyond simple intensity enhancement, direct control of the emission fields provides fine control

over emission characteristics such as directionality and polarization, making dielectric metasurfaces excellent candidates for compact and highly functional light sources [23–28].

While previous studies have demonstrated that integrating emitters with metasurfaces can enhance light emission and allow control over emission characteristics, most research has predominantly focused on optimizing the structural design of the dielectric metasurface alone—tuning parameters such as thickness, diameter, periodicity, and material composition [29–34]. In contrast, there has been relatively little experimental investigation into how the material properties of the emitter layer affect the overall emission performance. In the emitter-integrated dielectric metasurfaces, the emitter layer plays an important role in determining the achievable emission enhancement. Therefore, the emitter layer must be carefully considered during the design process to fully optimize emission behavior. Understanding the role of the emitter layer is thus not only scientifically important but also practically beneficial, enabling the development of optimized directional light sources.

In general, the emission characteristics of emitter-integrated dielectric metasurfaces can be analyzed using the reciprocity principle. According to the Lorentz reciprocity theorem, the far-field emission power of embedded light emitters can be obtained by integrating the electric-field intensity inside the emitting medium under external illumination [26, 35]. This approach is equivalent to the conventional dipole ensemble simulation, in which the far-field emission power from an ensemble of randomly positioned and oriented dipolar emitters is determined by integrating the total field enhancement at the dipole locations under incident light. However, the reciprocity-based calculations based on field enhancement simulations simplify emission calculations and are more straightforward to optimize.

According to temporal coupled-mode theory (TCMT), the field enhancement factor I in a resonant optical mode is given by $I \sim Q^2/(Q_{\mathrm{rad}}V_{\mathrm{eff}})$, where V_{eff} is the effective mode volume [36]. Here, the total Q factor is $Q = \omega_0/[2(\gamma_{\mathrm{rad}} + \gamma_{\mathrm{nr}})]$, where ω_0 is the resonant frequency, and γ_{rad} and γ_{nr} are the radiative and nonradiative damping rates, respectively. The radiative Q factor is defined as $Q_{\mathrm{rad}} = \omega_0/(2\gamma_{\mathrm{rad}})$. Then, the field enhancement reaches a maximum under the critical coupling condition $Q_{\mathrm{rad}} = Q_{\mathrm{nr}}$, as can be derived from the condition $dI/dQ_{\mathrm{rad}} = 0$. Because emission enhancement from the emitter-integrated metasurface (or *periodic* structures in general) can be calculated by integrating the field intensity in the emitter layer under incident light, the emission enhancement should also reach a maximum at the critical coupling condition. A similar argument has also been made in terms of spectral density of states (SDOS) $\rho(k, \omega)$ [37], where the same critical coupling condition (or Q-matching condition) was derived for the maximum enhancement of emission. Here, the wavevector k indicates a specific emission direction. Note that this is different from the local density of states (LDOS) $\rho(r, \omega)$ calculations, where the total emission of one dipole source is calculated into all directions.

The reciprocity analysis indicates that absorption losses in the emitter layer play a critical role because they determine the critical-coupling condition required for maximizing emission enhancement. Under critical coupling ($Q_{\mathrm{rad}} = Q_{\mathrm{nr}}$), the maximum achievable field enhancement is fundamentally limited by the nonradiative losses: $I_{\max} \propto 1/\gamma_{\mathrm{nr}}$ (thus, $I_{\max} \propto Q_{\mathrm{nr}}$). Nonradiative losses arise from material absorption at the emission wavelength, as well as from parasitic effects such as random scattering due to surface roughness and lateral energy leakage due to the finite size of the patterned region. Therefore, if other conditions (such as surface roughness and pattern size) remain the same, reducing the intrinsic absorption losses of the emitter layer can further increase the maximum achievable enhancement.

Here, we experimentally demonstrate that low absorption losses in the emitter layer can drastically increase the maximum achievable enhancement when different semiconductor quantum dots (QDs) are coated on the same dielectric metasurface. In our previous work, CdSe/ZnS QDs were used to investigate the effect of critical coupling on emission enhancement [36]. However, due to the nonnegligible absorption losses (i.e., $\kappa = \mathrm{Im}[\tilde{n}]$) in the QD layer, the observed enhancement was limited to approximately a 20–30-fold increase. In this study, we demonstrate highly directional emission with narrow angular divergence from QD-integrated dielectric metasurfaces. Particularly, we directly compare the emission characteristics in the visible region when InP/ZnS QDs and CdSe/ZnS QDs are coated on the same dielectric (TiO_2) metasurfaces. Through detailed simulations and experiments, we systematically investigate the role of the emitter layer in determining emission enhancement. While the absorption enhancement at the excitation laser wavelength remained unchanged, emission enhancement was maximized via critical coupling at the QD emission wavelength. We show that the lower intrinsic losses of the InP/ZnS QD layer enable dramatically improved emission performance, experimentally achieving extremely high enhancement (140-fold) in the vertical direction. Our experimental observations are consistent with critical-coupling behavior at the emission wavelength and exhibit excellent agreement with simulations.

Unlike most prior studies that focus primarily on metasurface geometry, our approach highlights how the emitter's intrinsic properties directly influence emission enhancement. Through detailed simulations and experiments, we develop a deeper understanding of emitter-integrated metasurfaces. These findings offer valuable insights into nanoscale emission engineering by enabling the co-design of the emitter and metasurface, and they contribute to the development of high-performance directional light sources.

2 | Results and Discussion

Figure 1a,b illustrate the schematic of the TiO_2-based dielectric metasurface, which consists of periodically arranged nanodisks fabricated on a quartz substrate. The metasurface has a periodicity of $p = 380$ nm, a TiO_2 disk diameter of $D_0 = 150$ nm, and a height of $h = 112$ nm. A QD layer is coated around the TiO_2 nanodisks. The disk size variation ΔD is defined as $\Delta D = D_0 - D$.

InP/ZnS QDs and CdSe/ZnS QDs exhibit different absorption losses at their emission wavelengths. Figure 1c,d show their refractive indices measured using ellipsometry (Elipso Technology, Elli-SE-UaM8). For the ellipsometry measurement, InP/ZnS QD and CdSe/ZnS QD layers were coated separately on bare quartz substrates. The corresponding QD photoluminescence (PL) spectra on bare substrates are provided in Figure S1 for reference. Both QD types exhibit PL in the visible region (around 550 nm). A notable distinction appears in the imaginary part of the refractive index

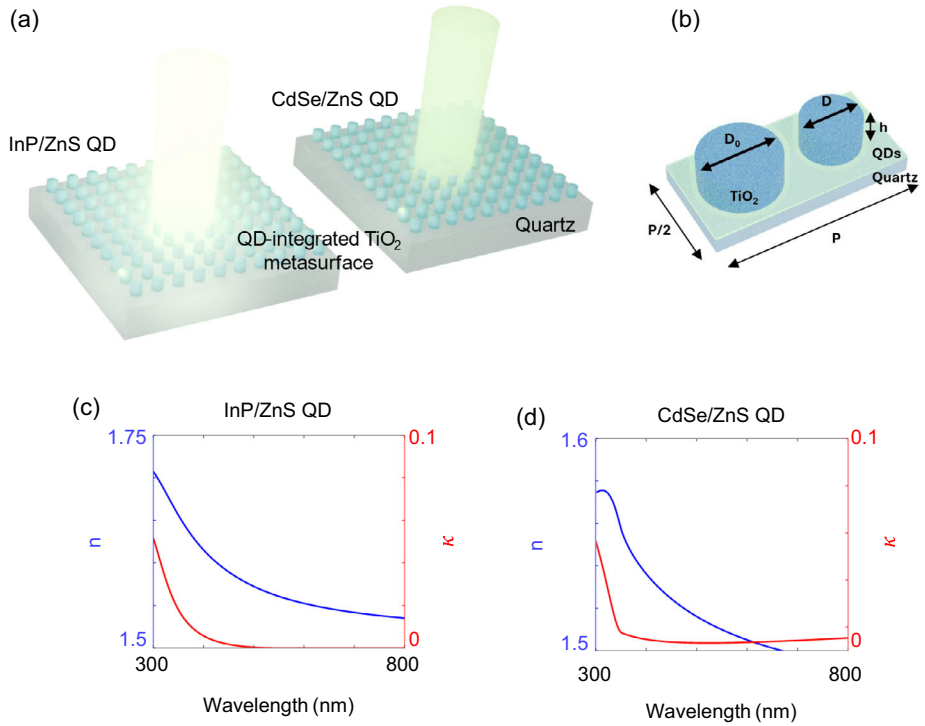

FIGURE 1 | Sample schematic and the optical characteristics of the quantum dot (QD) layer. (a) Schematic illustration of the dielectric metasurface integrated with InP/ZnS and CdSe/ZnS QDs. The metasurface structure consists of a periodic array of TiO_2 nanodisks on a quartz substrate. (b) Illustrative diagram of the dielectric metasurface unit cell geometry, showing the disk diameter ($D_0 = 150$ nm), periodicity ($P = 380$ nm), and disk height ($h = 112$ nm). The disk size variation ΔD is defined as $\Delta D = D_0 - D$. (c) Refractive index (n, blue) and extinction coefficient (κ, red) of (c) InP/ZnS QDs and (d) CdSe/ZnS QDs obtained from spectroscopic ellipsometry.

($\kappa = \mathrm{Im}[\tilde{n}]$): InP/ZnS QDs display extremely small absorption losses within the QD emission band, whereas CdSe/ZnS QDs retain a nonnegligible imaginary component ($\kappa \sim 0.0133$ at 550 nm), indicating larger absorption losses in the emission band. As we will show later, this difference in κ results in a pronounced contrast in emission enhancement when both QD types are spin-coated onto the same dielectric metasurface.

For the metasurface measurements, the TiO_2 disk arrays were fabricated using TiO_2 film deposition, electron-beam lithography, and reactive-ion etching (see the Experimental Section). Figure S2a shows the measured refractive index of the TiO_2 film. Figure S2b presents a scanning electron microscopy image of the fabricated TiO_2 disk array, and the corresponding height profile measured using atomic force microscopy further confirms the uniformity of the fabricated structures (Figure S2c). For the QD PL measurement, the fabricated TiO_2 metasurfaces were coated with InP/ZnS QDs and CdSe/ZnS QDs, respectively. The thickness of the QD layer (approximately 10 nm) was determined from ellipsometry measurements. Figure S3 displays an optical microscopy image of the QD-coated metasurface sample, which shows that arrays of patterns with varying ΔD values were fabricated on the same substrate.

We introduce the disk size variation to break the lattice symmetry along the x-direction, as shown in Figure 2a. This perturbation reduces the size of half of the disks and doubles the unit-cell size. Consequently, this period-doubling perturbation reduces the size of the first Brillouin zone by half. The inset in Figure 2b depicts the associated Brillouin-zone folding in momentum space. This symmetry breaking allows guided modes—which originally lie below the light line and are thus prevented from radiating into free space—to be folded into the continuum [38, 39]. Particularly, the band-edge modes located at the boundary of the first Brillouin zone (X) are folded back to the Γ point, enabling them to be excited by normally incident free-space light. This can also induce a strong electromagnetic field enhancement under normal incidence.

Figure 2b shows the band diagram for the InP/ZnS QD-integrated metasurface, obtained using the guided-mode expansion method [36]. The band diagram clearly shows that band folding induces a high-Q guided mode resonance (GMR) at the Γ point. Note that the band diagram is plotted on an energy scale along the y-axis. The air and substrate light lines in the unperturbed metasurface are also shown for reference. When the perturbation is set to $\Delta D = 10$ nm, Q_{rad} reaches approximately 450 at the Γ point. We note that, along the Γ-X direction (i.e., k_x direction), Q_{rad} decreases rapidly as it deviates from the Γ point. We also conducted reflectance spectra simulations with varying disk sizes ($\Delta D = 0$–20 nm) to illustrate how they evolve under relevant parameters (Figures S4 and S5). The simulated reflectance spectra clearly indicate that the optical mode we used is a y-polarized mode.

PL enhancement arises from both excitation (or absorption) enhancement and emission enhancement. The TiO_2 dielectric metasurface does not support optical resonances at our laser excitation wavelength (450 nm), and thus the absorption remains essentially unchanged for different perturbations ΔD (Figure S6). Therefore, in our QD-integrated metasurfaces, the observed PL enhancement with nonzero perturbation ΔD primarily results from emission enhancement by the optical mode at the QD

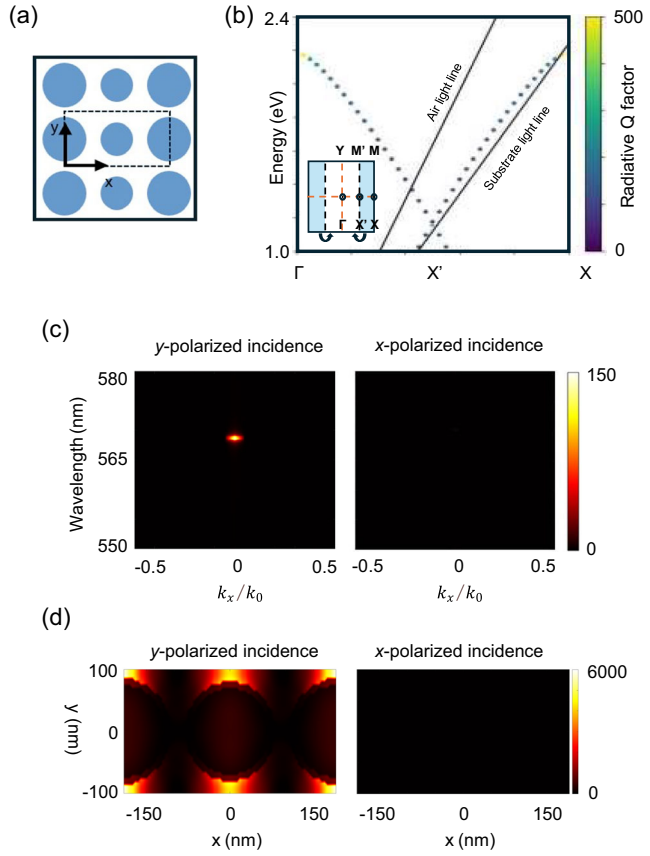

FIGURE 2 | Band structure and reciprocity-based calculation for the InP/ZnS QD-integrated metasurfaces. (a) Schematic of the period-doubling perturbation along the *x*-direction, where the TiO_2 metasurface is integrated with an additional 10 nm quantum dot layer. (b) Photonic band structure calculated using the guided-mode expansion (GME) method for $\Delta D = 10$ nm (assuming a lossless QD layer). The odd mode with respect to the *xz* mirror plane is shown. The air and substrate light lines of the unperturbed structure are shown for comparison. The inset shows the associated Brillouin zone folding. (c) Simulated field enhancement spectra along the k_x direction for $\Delta D = 10$ nm, showing strong polarization-dependent enhancement. The spectra are plotted as a function of normalized in-plane wavevector ($k_x/k_0 = \sin\theta$, where θ is the incidence angle) and wavelength. The measured refractive indices of TiO_2 and QD layers were used in the simulations, including the absorption losses of the QD layer. (d) Simulated electric field intensity ($|E/E_0|^2$) profile under *y*-polarized and *x*-polarized incidence (measured on the *x*-*y* plane in the middle of the TiO_2 disk).

emission wavelengths. In this case, based on Lorentz reciprocity, the emission enhancement can be evaluated by integrating the field intensity within the light-emitting QD layer under plane-wave illumination. The integrated electric-field intensity in the QD layer is normalized to the unperturbed case ($\Delta D = 0$) to enable direct comparison between simulation and PL measurements.

Figure 2c presents the reciprocity-based calculation results for the InP/ZnS QD-integrated TiO_2 metasurface. The field-enhancement spectra were calculated along the k_x direction (i.e., as a function of k_x and λ). As expected, only the *y*-polarized incidence exhibits pronounced enhancement features, since the excited GMR mode is *y*-polarized. Notably, strong field enhancement (and correspondingly strong emission enhancement via reciprocity) appears only near the Γ point because Q_{rad} decreases rapidly away from Γ. The electric field intensity profile is also simulated and shown in Figure 2d, where the field profile is measured on the *x*–*y* plane in the middle of the TiO_2 disk. The field profile clearly indicates that the field intensity is strongly enhanced between the TiO_2 disks where the emitters are located.

The period-doubled metasurface supports GMR modes along the k_y direction as well, owing to band folding from the guided modes along the *X*–*M* direction (Figure S7a). The corresponding band structure along Γ–*Y* is presented in Figure S7b for the InP/ZnS QD-coated metasurface. We find that the bands along the Γ–*X* and Γ–*Y* directions exhibit different curvatures and slopes. We further observe that along the Γ–*Y* direction, Q_{rad} decreases more slowly as the mode moves away from the Γ point. Figure S8 shows the reciprocity calculations along the Γ–*Y* direction (i.e., the k_y direction). The enhancement along the k_y direction persists over a broader portion of the mode dispersion. Significant enhancement appears only for *y*-polarized incidence again.

To directly evaluate the effect of critical coupling, we also performed reciprocity calculations under normal-incidence illumination (i.e., at the Γ point). The period-doubling perturbation provides a general pathway to approach critical coupling: Q_{rad} gradually decreases as the perturbation increases, while Q_{nr}, dominated by absorption in the QD layer, remains approximately constant. Figure 3a,b compares the field enhancement under normal incidence for InP/ZnS QDs and CdSe/ZnS QDs,

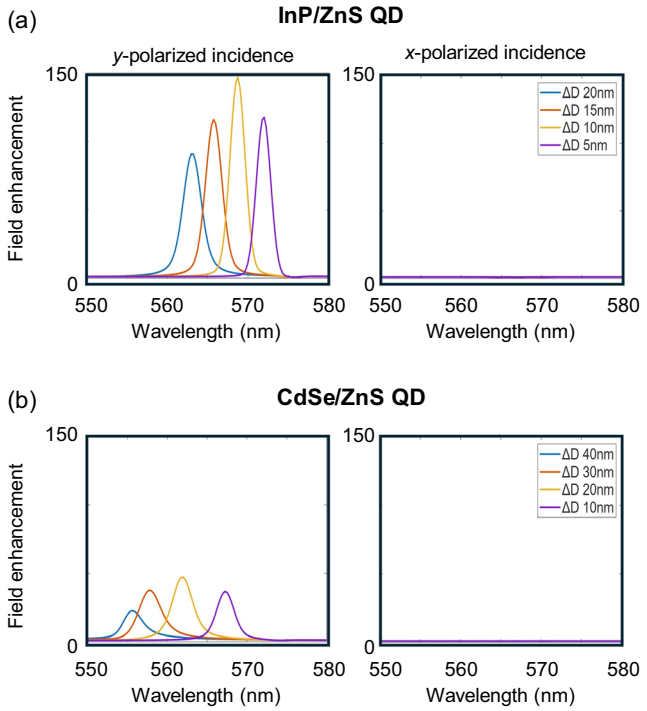

FIGURE 3 | Field enhancement calculation in the normal direction for InP/ZnS and CdSe/ZnS QD-integrated metasurfaces. (a) Simulated field enhancement spectra of the InP/ZnS QD layer for metasurfaces with varying disk diameters ($\Delta D = 5$–20 nm). (b) Simulated field enhancement spectra of the CdSe/ZnS QD layer for metasurfaces with varying disk diameters ($\Delta D = 10$–40 nm). The left and right panels show responses under *y*- and *x*-polarized incident light, respectively. The measured refractive indices of TiO_2 and QD layers were used in the simulations, including the absorption losses of the QD layer.

respectively, with varying disk diameters. The left panels correspond to *y*-polarized excitation, and the right panels correspond to *x*-polarized excitation. Both the InP/ZnS QD-integrated metasurface (top row) and the CdSe/ZnS QD-integrated metasurface (bottom row) exhibit strong polarization dependence, with pronounced enhancement observed only for *y*-polarized illumination. In both cases, the emission enhancement increases with ΔD, reaches a maximum, and then decreases as ΔD is further increased—consistent with the behavior expected from critical coupling. However, the optimal perturbation (i.e., the critical coupling condition yielding maximum field enhancement) differs between the two QD types due to their distinct absorption losses: $\Delta D = 10$ nm for InP/ZnS QDs and $\Delta D = 20$ nm for CdSe/ZnS QDs.

This critical coupling at specific ΔD values was directly verified by extracting the radiative and nonradiative Q factors (Q_{rad} and Q_{nr}) from the simulated reflectance spectra. Figure S9 shows the extracted Q factors for the InP/ZnS QD-coated metasurface. By fitting the simulated spectra to the reflectance formula derived from TCMT, Q_{rad} and Q_{nr} were obtained for different ΔD values. Q_{rad} gradually decreases with increasing ΔD due to the increased radiative loss with larger symmetry breaking, whereas Q_{nr}, determined by absorption in the QD layer, remains nearly constant. This directly confirms that the critical coupling condition ($Q_{rad} = Q_{nr}$) is satisfied at $\Delta D = 10$ nm for InP/ZnS QDs. In the same way, it can be shown that the critical-coupling condition is satisfied at $\Delta D = 20$ nm for CdSe/ZnS QDs.

Moreover, Figure 3 shows that the InP/ZnS QD-integrated metasurface with lower QD absorption losses exhibits a significantly higher maximum enhancement (~146.9 at $\Delta D = 10$ nm) compared to the CdSe/ZnS–coated metasurface (~47.1 at $\Delta D = 20$ nm). Note S1 presents a more *quantitative* analysis of the emission enhancement, considering the effect of both Q factor and mode volume V_{eff}. Because InP/ZnS and CdSe/ZnS QDs have different absorption losses, the two cases have different Q_{nr} values. Our quantitative analysis confirms that the absorption loss ($I_{max} \propto Q_{nr}$) is a major factor for the achievable maximum enhancement at critical coupling—that is, the imaginary part of the refractive index (κ) of the emitter layer strongly influences the field enhancement (and thus the emission enhancement). Therefore, all observations in Figure 3 are fully consistent with the expected critical-coupling behavior at the emission wavelength.

We conducted angle-resolved PL spectroscopy using a custom-built Fourier-plane setup (see Experimental Section), and the simulation results were compared with experimental measurements. Figure 4a presents the Fourier-plane (k_x–k_y) *y*-polarized PL images from the InP/ZnS QD-coated metasurface ($\Delta D = 10$ nm). The measurement was performed using a 570 nm bandpass filter, which selects a spectral window of approximately 565–575 nm. The two mode dispersions overlap at the Γ point ($k_x = 0$, $k_y = 0$), leading to strong emission enhancement in the vertical direction. Figure 4b shows the corresponding reciprocity calculation (i.e., the integrated field enhancement in the emitter layer averaged over the spectral band of 565–575 nm). Again, it is shown that the two bands overlap at the Γ point.

We also measured the angle-resolved PL spectra. Figure 5a,b compares the PL spectra for the InP/ZnS QD- and CdSe/ZnS QD-integrated metasurfaces, respectively, with varying disk sizes ($\Delta D = 0$–20 nm in 5 nm increments). In both cases, the QD PL intensity gradually increases with ΔD and reaches a maximum at a specific perturbation: $\Delta D = 10$ nm for InP/ZnS QDs and $\Delta D = 20$ nm for CdSe/ZnS QDs. As predicted by the simulations, the InP/ZnS QD-integrated metasurface exhibits significantly stronger PL enhancement compared with its CdSe/ZnS QD counterpart. Note that the same color scale (from 0 to 500) is used for both Figure 5a,b to facilitate comparison. Figure S10 presents Figure 5b for CdSe/ZnS QDs with a different color scale (from 0 to 200) to display the measured PL spectra more clearly. Both metasurfaces clearly show *y*-polarized emission. Consistent with the simulations (Figure 2c), the *y*-polarized PL spectra display a strongly enhanced PL spot at $k_x = 0$ (indicated by the arrow). In both cases, the QD-integrated metasurfaces produce highly directional, vertically emitted PL due to optical mode coupling. However, the InP/ZnS QD-integrated metasurface exhibits markedly stronger emission compared to the CdSe/ZnS QD sample. Moreover, the emission profile exhibits a narrow angular divergence of approximately 2° along the k_x axis (Figure S11), confirming the highly directional nature of the emission.

Figure 5c,d explicitly shows the emission enhancement in the vertical direction ($k_x = 0$). To quantify the enhancement, we normalized the measured PL intensity to that of the unperturbed structure ($\Delta D = 0$); the QD density on the patterned surface can reasonably be assumed to remain constant for small variations in disk size. Additionally, because the absorption at the excitation laser wavelength (450 nm) remains almost the same for all ΔDs

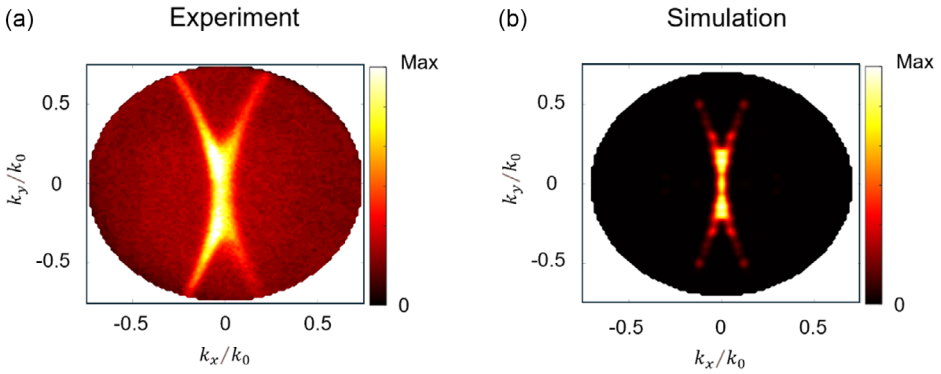

FIGURE 4 | Fourier-plane emission pattern from the InP/ZnS QD-integrated metasurfaces. (a) Experimentally measured PL image (*y*-polarized emission) at $\Delta D = 10$ nm. (b) The corresponding emission pattern obtained from the reciprocity calculation (averaged over the wavelength range of 565 ~ 575 nm).

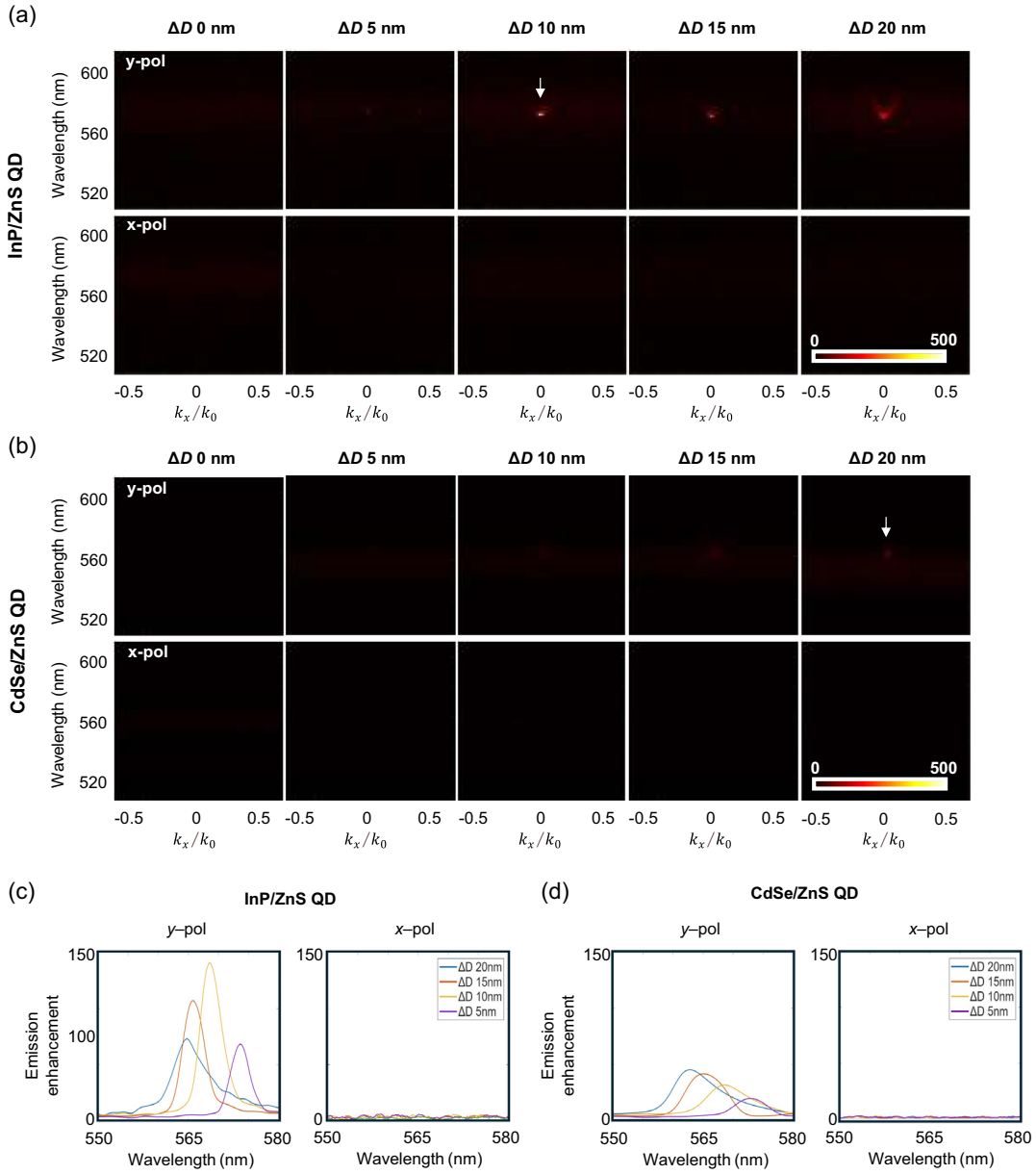

FIGURE 5 | Angle-resolved PL and emission enhancement. (a) Angle-resolved PL spectra of the metasurface integrated with InP/ZnS and (b) CdSe/ZnS QDs for different ΔD values (0 to 20 nm). The PL is collected under *y*- and *x*-polarized detection. The InP/ZnS QD exhibits a narrow angular divergence of ~2° along the k_x direction. Corresponding emission enhancement in the normal direction from (c) the InP/ZnS QD-integrated metasurface and (d) the CdSe/ZnS QD-integrated metasurface.

(Figure S6), the normalization of the PL spectrum to that at $\Delta D = 0$ also cancels out the contribution from the absorption enhancement; thus, emission enhancement factors can be extracted from the experimental PL measurement. Notably, the enhancement in the InP/ZnS QD-integrated metasurface reaches 140-fold under the optimal condition ($\Delta D = 10$ nm), which is substantially larger than the enhancement of the CdSe/ZnS QD counterpart (45-fold at $\Delta D =$ 20 nm). These experimental observations are in good agreement with the simulations. Table S1 in Supporting Information compares experimental demonstrations of QD emission enhancement at room temperature, where colloidal QDs are combined with photonic structures through spin-coating or similar methods. It clearly indicates that our result represents a very high emission enhancement.

Figure S12 directly compares the reciprocity calculations in Figure 3 with the experimental data in Figure 5c,d. Vertical dashed lines are intentionally added to compare the spectral positions at critical coupling. We find that the peak wavelengths in the simulation (upper row) and experiment (lower row) agree reasonably well. Overall, our results are fully consistent with the critical-coupling behavior, and the absorption losses in the emitter layer strongly influence the achievable emission enhancement. Our observations also experimentally confirm the *Q*-matching condition derived from the SDOS argument [37]. This strong correspondence between experiment and theory underscores the importance of matching the intrinsic properties of the emitter to the resonant characteristics of the metasurface to achieve optimal emission control.

Angle-resolved PL spectra were also measured along the Γ–*Y* direction for the InP/ZnS QD-integrated metasurface, as shown in Figure S13. The PL intensity varies systematically with the TiO_2 disk diameter and again reaches its maximum at $\Delta D = 10$ nm. In contrast to the Γ–*X* direction, the PL band along the Γ–*Y* direction is more extended in the k_y direction. This experimental result is again in good agreement with the simulations, confirming the distinct emission behavior along the two directions.

InP/ZnS QDs have recently attracted much attention as cadmium-free, environmentally friendly alternatives. However, their emission linewidth is typically broader than those of CdSe/ZnS QDs, as shown in Figure S1. By combining InP/ZnS QDs with dielectric metasurfaces, strong emission enhancement can be achieved via mode coupling to high-*Q* optical resonances, resulting in a much narrower emission linewidth. This represents another interesting aspect of InP/ZnS QD-integrated dielectric metasurfaces.

3 | Conclusion

We experimentally demonstrated highly enhanced directional and polarized emission from QD-integrated metasurfaces. By systematically varying the TiO_2 disk size, we verified that the emission enhancement reaches its maximum under the critical coupling condition. Our combined experimental and theoretical studies highlight the crucial role of the emitter layer in optimizing the emission properties of the emitter-integrated metasurfaces. We showed that the material properties of the emitter—such as its intrinsic losses—significantly influence the achievable emission enhancement. All these findings are fully consistent with critical-coupling behavior. Emitter-integrated metasurfaces can offer enhanced functionality for compact light sources without the need for external, bulky optical components. Such compact light sources with high directionality and controlled polarization are promising for applications in displays, optical communications, sensing, and imaging.

4 | Experimental Section

4.1 | Sample Fabrication

Dielectric metasurfaces were fabricated by depositing a 112 nm-thick TiO_2 film onto quartz substrates using radio-frequency (RF) sputtering. The TiO_2 layer was patterned via electron-beam lithography (EBL). A chromium (Cr) hard mask was then deposited and patterned using a lift-off process. The nanostructures were etched using inductively coupled plasma reactive ion etching (ICP-RIE) with a gas mixture of Ar, CF_4, and BCl_3, and the Cr mask was subsequently removed using a chromium etchant (Sigma–Aldrich). After fabrication, a QD solution (1 mg/mL in chloroform) was spin-coated on the TiO_2 metasurface sample at 4500 rpm for 60 s, followed by washing with isopropyl alcohol (IPA) to ensure uniform coating. InP/ZnS QDs were purchased from Sigma–Aldrich (776793), while CdSe/ZnS QDs were purchased from PlasmaChem (PL-QD-O-550).

4.2 | Numerical Simulations

The electric field enhancement around the metasurface structure was calculated using Rigorous Coupled-Wave Analysis (RCWA) [40]. Far-field emission enhancement was estimated based on the Lorentz reciprocity principle by integrating the electric field intensity within the emitter layer under external excitation. The photonic band structure and radiative *Q* factors were simulated using the guided-mode expansion (GME) method, implemented in the legume simulation package [41, 42] The current version of legume supports only nondispersive materials with constant refractive indices. Except for the band structure analysis, all other numerical simulations in this study—including field enhancement and reflectance spectra—were performed with RCWA using experimentally measured refractive indices.

4.3 | Optical Characterization

The angle-resolved reflectance and PL spectra were obtained using a custom-designed Fourier-plane optical setup (Figure S14) [43, 44]. In this configuration, the back focal plane of the microscope objective was projected, and the spectral information at different angles was captured by employing the slit of a monochromator as the line aperture positioned in the Fourier plane. For the reflectance measurement, a collimated white-light source was directed onto the sample surface through a high-NA objective (NA = 0.75). The reflected intensity was recorded, and the raw spectra were subsequently normalized against the baseline reflectance of a smooth silver film to eliminate background contributions. PL spectra were measured under excitation with a linearly polarized diode laser operating at 450 nm. The excitation laser beam had a power of 10 μW, and each spectrum was integrated over a 5-second interval. All experiments were carried out under ambient room-temperature conditions.

Acknowledgments

The authors acknowledge the support from the National Research Foundation (NRF) of Korea: 2023R1A2C1004674 (RS-2026-25476170) and 2022M3H4A1A04096465 (RS-2022-NR068230). We thank the UNIST Office of Research Facilities and Training (ResFacT) for support of using the equipment.

Funding

This study was supported by the National Research Foundation of Korea (RS-2026-25476170 and RS-2022-NR068230).

Conflicts of Interest

The authors declare no conflicts of interest.

Data Availability Statement

The data that support the findings of this study are available from the corresponding author upon reasonable request.

References

1. X. Fu, Y. Mehta, Y.-A. Chen, et al., "Directional Polarized Light Emission from Thin-Film Light-Emitting Diodes," *Advanced Materials* 33 (2021): 2006801.

2. Y. Mohtashami, L. K. Heki, M. S. Wong, et al., "Metasurface Light-Emitting Diodes with Directional and Focused Emission," *Nano Letters* 23 (2023): 10505.

3. Y. Wang, J. Tian, M. Klein, G. Adamo, S. T. Ha, and C. Soci, "Directional Emission from Electrically Injected Exciton–Polaritons in Perovskite Metasurfaces," *Nano Letters* 23 (2023): 4431.

4. S.-C. An, Y. Lim, K. Y. Lee, et al., "Topological Exciton Polaritons in Compact Perovskite Junction Metasurfaces," *Advanced Functional Materials* 34 (2024): 2313840.

5. M. Jeong, B. Ko, C. Jung, et al., "Printable Light-Emitting Metasurfaces with Enhanced Directional Photoluminescence," *Nano Letters* 24 (2024): 5783.

6. Y. Chung, G. Baek, J. Min, S. Park, S. Woo, and M. Lee, "Tailoring Directional Emission of Colloidal Quantum Dots *via* Mode Coupling with Photonic Crystals," *Nanoscale* 17 (2025): 20880.

7. T. Zhan, K. Yin, J. Xiong, Z. He, and S.-T. Wu, "Augmented Reality and Virtual Reality Displays: Perspectives and Challenges," *iScience* 23 (2020): 101397.

8. Z. Liu, D. Wang, H. Gao, M. Li, H. Zhou, and C. Zhang, *Advanced Photonics* 5 (2023): 034001.

9. Y.-H. Lee, T. Zhan, and S.-T. Wu, "Prospects and Challenges in Augmented Reality Displays," *Virtual Reality & Intelligent Hardware* 1 (2019): 10.

10. A. I. Kuznetsov, A. E. Miroshnichenko, M. L. Brongersma, Y. S. Kivshar, and B. Luk'yanchuk, "Optically Resonant Dielectric Nanostructures," *Science* 354 (2016): aag2472.

11. Y. S. Kivshar and A. Miroshnichenko, *OPN* 28 (2017): 24.

12. S. Murai, G. W. Castellanos, T. V. Raziman, A. G. Curto, and J. G. Rivas, "Enhanced Light Emission by Magnetic and Electric Resonances in Dielectric Metasurfaces," *Advanced Optical Materials* 8 (2020): 1902024.

13. L. Zhu, S. Yuan, C. Zeng, and J. Xia, "Manipulating Photoluminescence of Carbon G-center in Silicon Metasurface with Optical Bound States in the Continuum," *Advanced Optical Materials* 8 (2020): 1901830.

14. Z. Zhang, C. Xu, C. Liu, et al., "Dual Control of Enhanced Quasi-Bound States in the Continuum Emission from Resonant c-Si Metasurfaces," *Nano Letters* 23 (2023): 7584.

15. E. Csányi, Y. Liu, S. D. Rezaei, et al., "Engineering and Controlling Perovskite Emissions via Optical Quasi-Bound-States-in-the-Continuum," *Advanced Functional Materials* 34 (2024): 2309539.

16. A. Arbabi, Y. Horie, M. Bagheri, and A. Faraon, "Dielectric Metasurfaces for Complete Control of Phase and Polarization with Subwavelength Spatial Resolution and High Transmission," *Nature Nanotechnology* 10 (2015): 937.

17. S. T. Ha, Y. H. Fu, N. K. Emani, et al., "Directional Lasing in Resonant Semiconductor Nanoantenna Arrays," *Nature Nanotechnology* 13 (2018): 1042.

18. M. I. Shalaev, J. Sun, A. Tsukernik, A. Pandey, K. Nikolskiy, and N. M. Litchinitser, "High-Efficiency All-Dielectric Metasurfaces for Ultracompact Beam Manipulation in Transmission Mode," *Nano Letters* 15 (2015): 6261.

19. J. Guo, R. Jin, Z. Fu, et al., "Topologically Engineered High- *Q* Quasi-BIC Metasurfaces for Enhanced Near-Infrared Emission in PbS Quantum Dots," *Nano Letters* 25 (2025): 2357.

20. C. Zhou, M. Zhou, Z. Fu, et al., "Ultrahigh-Q Quasi-BICs via Precision-Controlled Asymmetry in Dielectric Metasurfaces," *Nano Letters* 25 (2025): 5916.

21. L. Liu, S. Ni, F. Zhu, et al., "Highly Sensitive Multicolor Uncooled Photoresponse and Imaging Based on Symmetry Breaking Heterojunction," *InfoMat* 7 (2025): e12641.

22. X. Li, J. Wang, F. Yu, et al., "Nonlinear Memristive Computational Spectrometer," *Light: Science & Applications* 14 (2025): 47.

23. E. Khaidarov, Z. Liu, R. Paniagua-Domínguez, et al., "Control of LED Emission with Functional Dielectric Metasurfaces," *Laser & Photonics Reviews* 14 (2020): 1900235.

24. S. Kim, B. H. Woo, S.-C. An, et al., "Topological Control of 2D Perovskite Emission in the Strong Coupling Regime," *Nano Letters* 21 (2021): 10076.

25. X. Zhang, Y. Liu, J. Han, Y. S. Kivshar, and Q. Song, "Chiral Emission from Resonant Metasurfaces," *Science* 377 (2022): 1215.

26. Y. Lim, I. C. Seo, S.-C. An, et al., "Maximally Chiral Emission via Chiral Quasibound States in the Continuum," *Laser & Photonics Reviews* 17 (2023): 2200611.

27. S. Kim, S.-C. An, Y. Kim, et al., "Chiral Electroluminescence from Thin-Film Perovskite Metacavities," *Science Advances* 9 (2023): eadh0414.

28. J. Han, H. Jang, Y. Lim, S. Kim, J. Lee, and Y. C. Jun, "Chiral Emission from Optical Metasurfaces and Metacavities," *Advanced Photonics Research* 5 (2024): 2400060.

29. Y. T. Lin, A. Hassanfiroozi, W.-R. Jiang, M.-Y. Liao, W.-J. Lee, and P. C. Wu, "Photoluminescence Enhancement with All-dielectric Coherent Metasurfaces," *Nanophotonics* 11 (2022): 2701.

30. I. Staude, T. Pertsch, and Y. S. Kivshar, "All-Dielectric Resonant Meta-Optics Lightens up," *ACS Photonics* 6 (2019): 802.

31. C. W. Hsu, B. Zhen, A. D. Stone, J. D. Joannopoulos, and M. Soljačić, "Bound States in the Continuum," *Nature Reviews Materials* 1 (2016): 1.

32. K. Koshelev, S. Kruk, E. Melik-Gaykazyan, et al., "Subwavelength Dielectric Resonators for Nonlinear Nanophotonics," *Science* 367 (2020): 288.

33. N. Ganesh, W. Zhang, P. C. Mathias, et al., "Enhanced Fluorescence Emission from Quantum Dots on a Photonic Crystal Surface," *Nature Nanotechnology* 2 (2007): 515.

34. P. Lodahl, A. F. van Driel, I. S. Nikolaev, et al., "Controlling the Dynamics of Spontaneous Emission from Quantum Dots by Photonic Crystals," *Nature* 430 (2004): 654.

35. M. Ramezani, G. Lozano, M. A. Verschuuren, and J. Gómez-Rivas, "Modified Emission of Extended Light Emitting Layers by Selective Coupling to Collective Lattice Resonances," *Physical Review B* 94 (2016): 125406.

36. J. Han, Y. Lim, J. Lee, S. Kim, and Y. C. Jun, "Maximized Enhancement of Polarized and Unpolarized Emissions via Critical Coupling in Brillouin Zone Folding Metasurfaces," *Laser & Photonics Reviews* 19 (2025): 2401923.

37. B. Zhen, S.-L. Chua, J. Lee, et al., "Enabling Enhanced Emission and Low-Threshold Lasing of Organic Molecules Using Special Fano Resonances of Macroscopic Photonic Crystals," *Proceedings of the National Academy of Sciences* 110 (2013): 13711.

38. W. Wang, Y. K. Srivastava, T. C. Tan, Z. Wang, and R. Singh, "Brillouin Zone Folding Driven Bound States in the Continuum," *Nature Communications* 14 (2023): 2811.

39. K. Sun, W. Wang, and Z. Han, "High- Q Resonances in Periodic Photonic Structures," *Physical Review B* 109 (2024): 085426.

40. J. P. Hugonin and P. Lalanne, arXiv 2021, arXiv, 2101.00901.

41. S. Zanotti, M. Minkov, D. Nigro, D. Gerace, S. Fan, and L. C. Andreani, "Legume: A Free Implementation of the Guided-Mode Expansion Method for Photonic Crystal Slabs," *Computer Physics Communications* 304 (2024): 109286.

42. M. Minkov, I. A. D. Williamson, L. C. Andreani, et al., "Inverse Design of Photonic Crystals through Automatic Differentiation," *ACS Photonics* 7 (2020): 1729.

43. I. C. Seo, S. Kim, B. H. Woo, I.-S. Chung, and Y. C. Jun, "Fourier-plane Investigation of Plasmonic Bound States in the Continuum and Molecular Emission Coupling," *Nanophotonics* 9 (2018): 4565.

44. Y. Zhang, M. Zhao, J. Wang, et al., "Momentum-Space Imaging Spectroscopy for the Study of Nanophotonic Materials," *Science Bulletin* 66 (2021): 824.

Supporting Information

Additional supporting information can be found online in the Supporting Information section.